

Towards measuring supermassive black hole masses with interferometric observations of the dust continuum

GRAVITY Collaboration^{*}: A. Amorim^{15,17}, G. Bourdarot¹, W. Brandner¹⁸, Y. Cao¹, Y. Clénet², R. Davies¹, P. T. de Zeeuw^{1,13}, J. Dexter^{20,1}, A. Drescher¹, A. Eckart^{3,14}, F. Eisenhauer¹, M. Fabricius¹, N. M. Förster Schreiber¹, P. J. V. Garcia^{11,16,17}, R. Genzel^{1,4}, S. Gillessen¹, D. Gratadour^{2,21}, S. Hönig⁵, M. Kishimoto⁶, S. Lacour^{2,12}, D. Lutz¹, F. Millour⁷, H. Netzer⁸, T. Ott¹, T. Paumard², K. Perraut⁹, G. Perrin², B. M. Peterson²², P. O. Petrucci⁹, O. Pfuhl¹², M. A. Prieto¹⁹, D. Rouan², D. J. D. Santos¹, J. Shangguan¹, T. Shimizu¹, A. Sternberg^{8,10}, C. Straubmeier³, E. Sturm¹, L. J. Tacconi¹, K. R. W. Tristram¹¹, F. Widmann¹, and J. Woillez¹²

(Affiliations can be found after the references)

September 30, 2022

ABSTRACT

This work focuses on active galactic nuclei (AGNs), and the relation between the sizes of the hot dust continuum and the broad-line region (BLR). We find that the continuum size measured using optical/near-infrared interferometry (OI) is roughly twice that measured by reverberation mapping (RM). Both OI and RM continuum sizes show a tight relation with the $H\beta$ BLR size with only an intrinsic scatter of 0.25 dex. The masses of supermassive black holes (BHs) can hence be simply derived from a dust size in combination with a broad line width and virial factor. Since the primary uncertainty of these BH masses comes from the virial factor, the accuracy of the continuum-based BH masses is close to those based on the RM measurement of the broad emission line. Moreover, the necessary continuum measurements can be obtained on a much shorter timescale than those required monitoring for RM, and are also more time efficient than those needed to resolve the BLR with OI. The primary goal of this work is to demonstrate measuring the BH mass based on the dust continuum size with our first calibration of the $R_{\text{BLR}}-R_{\text{d}}$ relation. The current limitation and caveats are discussed in detail. Future GRAVITY observations are expected to improve the continuum-based method and have the potential to measure BH masses for a large sample of AGNs in the low-redshift Universe.

Key words. galaxies: active – galaxies: nuclei – galaxies: Seyfert – quasars: supermassive black holes

1. Introduction

Measuring the mass of supermassive black holes (BHs) is challenging as this requires resolving stellar or gas dynamics inside the BH's sphere of influence (e.g. Thomas et al. 2004; Onken et al. 2014; Saglia et al. 2016; Hicks & Malkan 2008; Davis 2014; Onishi et al. 2017; Boizelle et al. 2019). In active galactic nuclei (AGNs) with broad recombination lines, the reverberation mapping (RM) method has been developed to measure the size of the broad-line region (BLR) and hence lead to the measurement of the BH mass (Blandford & McKee 1982; Peterson 1993; Peterson et al. 2004). By monitoring the variability of the UV/optical continuum and an emission line, typically $H\beta$, the BLR size can be obtained from the RM method. Assuming that the BLR is a virialized system, one can calculate the BH mass,

$$M_{\text{BH}} = f \frac{R_{\text{BLR}}(\Delta V)^2}{G}, \quad (1)$$

where R_{BLR} is the BLR radius, ΔV is the velocity width of the broad emission line, f is the corresponding virial factor, and G is the gravitational constant. The FWHM or second moment (σ_{line})

^{*} GRAVITY is developed in a collaboration by the Max Planck Institute for Extraterrestrial Physics, LESIA of Observatoire de Paris/Université PSL/CNRS/Sorbonne Université/Université de Paris and IPAG of Université Grenoble Alpes /CNRS, the Max Planck Institute for Astronomy, the University of Cologne, the CENTRA - Centro de Astrofísica e Gravitação, and the European Southern Observatory. Corresponding authors: J. Shangguan (shangguan@mpe.mpg.de) and Y. Cao (ycao@mpe.mpg.de)

of the broad line is usually used as ΔV . The virial factor f depends on the geometry, kinematics, and inclination of the BLR clouds and is likely different from object to object. For example, the virial factor is 0.75 assuming an isotropic velocity distribution of Keplerian motion (Netzer 1990). The mean virial factor, $\langle f \rangle$, can be calibrated using nearby AGNs assuming that the AGN and quiescent galaxies follow the same $M_{\text{BH}}-\sigma_*$ relation (e.g. Onken et al. 2004; Woo et al. 2010; Graham et al. 2011; Grier et al. 2013; Ho & Kim 2014). This method based on RM measurements has been used successfully for many years, despite potential biases and caveats in the virial factor calibration (Shankar et al. 2019). For a particular source, the uncertainty in f may come from its unknown inclination angle and other effects such as the radiation pressure (Collin et al. 2006; Mejía-Restrepo et al. 2018).

Moreover, a scaling relation between the BLR radius and AGN luminosity was discovered from RM measurements (Kaspi et al. 2000; Dalla Bontà et al. 2020, and references therein). This $R-L$ relation enables one to estimate the BH mass only with the AGN luminosity and the FWHM of a broad emission line from single-epoch spectra (Shen 2013). Thanks to its simplicity, the single-epoch method has been widely used with different broad lines in the UV and optical, although the uncertainty is around 0.5 dex or above (e.g. Vestergaard & Peterson 2006). Other methods have been developed to estimate the BH mass and tested against the RM measured BH mass. For example, the coronal line [Si VI]1.963 μm can be used to estimate the BH mass with an uncertainty of about 0.5 dex (Prieto et al. 2022).

Recently, the BLRs of three AGNs have been spatially resolved by GRAVITY, a second-generation Very Large Telescope Interferometer (VLTI) instrument (Gravity Collaboration et al. 2018, 2020a, 2021b). GRAVITY has greatly improved the sensitivity of earlier efforts and has been able to combine all four of the 8-m Unit Telescope (UT) beams to yield six simultaneous baselines (Gravity Collaboration et al. 2017). With a few hours of on-source exposure, GRAVITY measures the differential phase signal of a broad emission line in the near-infrared (NIR) K -band, which reflects the offsets of the photocenters from the center of the continuum emission in each wavelength channel (Petrov et al. 2001; Marconi et al. 2003). The BLR size is then inferred from the differential phase data by fitting a dynamical BLR model such as the widely used Pancoast et al. (2014a) model. The GRAVITY-measured BLR size and BH mass are in good agreement with RM measurements (Gravity Collaboration et al. 2021b,a).

GRAVITY can also resolve the size of the NIR continuum emission of the AGN, which comes from the thermal radiation of hot dust that is reprocessing the UV/optical continuum from the accretion disk (e.g. Rees et al. 1969; Barvainis 1987). Spatial sizes of the dust continuum emission can be measured by both continuum RM (e.g. Clavel et al. 1989; Baribaud et al. 1992; Glass 1992; Sitko et al. 1993; Minezaki et al. 2004; Suganuma et al. 2006; Koshida et al. 2014; Pozo Nuñez et al. 2014, 2015; Mandal et al. 2018; Minezaki et al. 2019; Sobrino Figaredo et al. 2020; Mandal et al. 2021a,b) as well as optical/NIR interferometry (OI; Swain et al. 2003; Wittkowski et al. 2004; Kishimoto et al. 2009, 2011; Gravity Collaboration et al. 2020b; Leftley et al. 2021). Similar to the BLR size, the dust continuum size also scales with the AGN luminosity $\propto L^{0.5}$ (Suganuma et al. 2006; Kishimoto et al. 2011; Koshida et al. 2014; Minezaki et al. 2019; Gravity Collaboration et al. 2020b). Such a relation is expected if the dust temperature and the inner radius of the dust distribution are determined by radiation equilibrium and dust sublimation, respectively (Barvainis 1987; Kishimoto et al. 2007). The dust continuum RM radius is a factor of four or five larger than the BLR radius (Koshida et al. 2014) and is consistent with BLR models that place hot dust on the outskirts of the BLR (e.g. Wang et al. 2017; Baskin & Laor 2018). Moreover, RM-measured dust continuum sizes are systematically smaller than those measured from OI, likely because the RM size is weighted by the time lag over the emitting region while the OI size is weighted by the intensity of hot dust emission (Koshida et al. 2014; Kishimoto et al. 2011; Gravity Collaboration et al. 2020b).

GRAVITY can observe the dust continuum independently of the full spectroastrometric measurements and has demonstrated excellent efficiency (e.g. $\lesssim 1$ hour per source; Gravity Collaboration et al. 2020b and in preparation). Establishing a link between the BLR and dust continuum size will enable BH mass estimations from these more accessible dust continuum observations. In this work, we investigate the correlation between BLR and dust continuum size in the context of estimating the BH mass. The four methods discussed in this paper are:

1. Reverberation mapping of the broad emission line, where a sequence of measurements over months or years, yielding the time delay for variations in the broad-line emission, leads to an estimate R_{BLR} ; and hence, via Equation (1), the BH mass (Peterson 2014). This method has enabled empirical calibration of a sample-average virial factor $\langle f \rangle$. More recently, the velocity resolved RM data can constrain a BLR dynamical model and enable the estimation of f for individual sources (e.g. Pancoast et al. 2014a,b).
2. The single-epoch method, where R_{BLR} is estimated from a single measurement of the AGN luminosity via the relation between these quantities (Shen 2013; Dalla Bontà et al. 2020). This method relies on Equation (1) and the virial factor calibrated via RM.
3. Continuum size measurements, the method introduced in this paper, where R_{BLR} is estimated from an interferometric measurement of R_d . Like the single-epoch method, this also relies on Equation (1) and a pre-calibration of the virial factor.
4. Spectrally resolved differential phase measurements of the broad-line emission. Using the interferometric data as constraints on a dynamical BLR model allows one to derive BH mass; and hence also infer a value of the virial factor for individual sources that is independent of RM (Gravity Collaboration et al. 2020a).

We show that the $H\beta$ BLR size scales tightly with the dust continuum size, which allows us to estimate the BH mass from the dust continuum size with an uncertainty similar to the RM BLR method. We discuss the prospects of this method for BH mass estimations in the low-redshift Universe, especially with the upgrade of GRAVITY in Section 5. This work adopts the following parameters for a Λ CDM cosmology: $\Omega_m = 0.308$, $\Omega_\Lambda = 0.692$, and $H_0 = 67.8 \text{ km s}^{-1} \text{ Mpc}^{-1}$ (Planck Collaboration et al. 2016).

2. Samples

2.1. Dust continuum measurements

We collect type 1 AGNs with dust continuum sizes measured by RM and/or OI in Table 1. The dust continuum sizes based on K -band RM observations are mainly measured by Koshida et al. (2014). Minezaki et al. (2019) summarized the results of Koshida et al. (2014) in their Table 6, using the power index $\alpha = 0.1$ to remove the NIR emission from the accretion disk (i.e. $f_\nu \propto \nu^\alpha$) to be consistent with their primary results. The assumption of the power index may introduce a $\lesssim 10\%$ difference in the time lag, which is typically not significant compared to the measurement uncertainty (Koshida et al. 2014; Minezaki et al. 2019). We, therefore, adopt the time lags from Minezaki et al. (2019) whenever available. The K -band time lag probes the dust emission size at shorter wavelength for higher redshift sources, so we prefer not to include AGNs much higher than $z \approx 0.2$ (see also Section 3.3). Minezaki et al. (2019) also reported K -band continuum RM measurements for a sample of quasars at $z \approx 0.1$ – 0.6 , most of which do not have $H\beta$ RM measurements. We only include three quasars from this sample, PG 0844+349, PG 0953+414, and PG 1613+658, because they have $H\beta$ RM measurements and are valuable to study the relation of the dust continuum and BLR sizes. K -band RM measurements of the other targets, e.g. 3C 120 (Ramolla et al. 2018) and H 0507+164 (Mandal et al. 2018), are collected from individual papers.

We also find 23 AGNs with dust continuum sizes measured by OI, which consists of Keck (Kishimoto et al. 2009, 2011) and recent VLTI/GRAVITY observations (Gravity Collaboration et al. 2020b and in preparation). Kishimoto et al. measured the dust continuum size by fitting squared visibility amplitudes (V^2) with a thin-ring model. They corrected the influence of the accretion disk assuming a point source contribution to the visibilities. Gravity Collaboration et al. (2020b) measured the dust continuum size by fitting a Gaussian model to the V^2 . They converted the Gaussian FWHM to the thin-ring radius and corrected the radius assuming a 20% contribution of the coherent flux from the accretion disk. Recent GRAVITY observations measured the

Table 1. Physical properties of AGNs with dust continuum size measurements

Name	Redshift	R_d (RM) (ld)	Ref.	R_d (OI) (ld)	Ref.	R_{BLR} (ld)	FWHM (km s ⁻¹)	$\log \lambda L_\lambda$ (5100 Å) (erg s ⁻¹)	Ref.	$\log M_{BH}$ (M_\odot)	$\log \lambda_{Edd}$
(1)	(2)	(3)	(4)	(5)	(6)	(7)	(8)	(9)	(10)	(11)	(12)
Mrk 335	0.0258	167.5±6.0	1	185±49	2	14.0±4.0	1707±79	43.8	3	6.90±0.13	-0.29
UGC 545	0.0612	707±77	4	37.2±4.7	1131±37	44.5	5	6.97±0.06	0.39
Mrk 590 ^{a,b}	0.0264	33.5±4.2	1	25.6±5.9	2716±202	43.5	3	7.57±0.12	-1.21
3C 120	0.0330	94.4±5.5	6	379±85	2	26.2±7.7	2472±729	44.0	3	7.49±0.29	-0.64
H0507+164	0.0179	35±11	7	3.0±1.2	4062±247	42.6	8	6.99±0.18	-1.57
Akn 120	0.0327	138±18	1	387±77	4	39.5±8.2	6077±147	43.9	3	8.45±0.09	-1.73
MCG+08-11-011	0.0205	72.7±1.6	1	15.7±0.5	4139±207	43.3	3	7.72±0.05	-1.54
Mrk 6 ^c	0.0195	214±60	9	18.5±2.5	5457±16	43.6	10	8.03±0.06	-1.55
Mrk 79	0.0222	67.7±4.8	1	15.6±5.0	4793±145	43.7	3	7.84±0.14	-1.31
PG 0844+349	0.0640	99±11	1	32.3±13.6	2694±58	44.2	3	7.66±0.18	-0.59
Mrk 110	0.0353	116.6±6.3	1	25.6±8.1	1634±83	43.7	3	7.13±0.14	-0.61
PG 0953+414	0.2341	566±44	1	150.1±22.1	3071±27	45.2	3	8.44±0.06	-0.40
NGC 3227	0.0038	14.37±0.70	1	45.0±7.2	4	3.8±0.8	4112±206	42.2	3	7.10±0.10	-2.00
NGC 3516 ^a	0.0088	72.7±4.6	1	11.7±1.3	5384±269	42.8	3	7.82±0.06	-2.18
NGC 3783	0.0097	76.3±14.1	11	131±20	2	9.6±0.7	4486±35	43.0	12	7.58±0.03	-1.70
NGC 4051	0.0023	16.30±0.57	1	38.1±6.0	13	2.1±0.8	1076±277	41.9	3	5.68±0.28	-0.92
NGC 4151 ^a	0.0033	46.11±0.44	1	44.1±8.3 ^c	9	6.6±1.0	6371±150	42.1	3	7.72±0.07	-2.77
3C 273	0.1583	409±41	14	675±126	2	146.8±10.2	3314±59	45.9	3	8.50±0.03	0.28
NGC 4593	0.0083	41.82±0.90	1	54.8±8.8	4	4.0±0.8	5142±572	42.6	3	7.31±0.13	-1.84
MCG-6-30-15	0.0078	19.6±4.9	15	5.7±1.8	1947±58	41.6	3	6.63±0.14	-2.13
NGC 5548	0.0172	61.21±0.30	1	13.9±8.7	7256±2203	43.3	3	8.15±0.38	-2.00
Mrk 817	0.0313	92.6±8.9	1	19.9±8.3	5348±536	43.7	3	8.05±0.20	-1.45
PG 1613+658	0.1211	334±40	1	40.1±15.1	9074±103	44.8	3	8.81±0.16	-1.19
Z 229-15	0.0279	20.4±5.8	16	3.9±0.8	3350±72	42.9	17	6.93±0.09	-1.18
Mrk 509	0.0344	121.3±1.6	1	297±31	2	79.6±5.8	3015±2	44.2	3	8.15±0.03	-1.11
NGC 7469	0.0163	85.29±0.43	1	10.8±2.4	4369±6	43.5	3	7.60±0.10	-1.24
NGC 1365 ^a	0.0055	38.1±4.8	2	...	1586±465	41.9	2 ^f ,18
IRAS 03450+0055	0.0315	157.4±5.9	1	3098±55	43.9	1,19
IRAS 09149-6206 ^d	0.0573	482±49	2	...	4281±121	45.0	20,21	8.06±0.25	-0.26
Mrk 1239	0.0199	189±30	4	...	830±10	44.5	22 ^f
WPVS 48	0.0370	70.8±4.6	23	1890±60	43.6	24
Mrk 744	0.0091	19.9±2.2	1	5616±129	41.8	1,21 ^g
HE 1029-1401	0.0858	880±133	4	...	5684±284	44.6	21
GQ Com	0.1650	210±40	25	5036±252	44.6	26
Mrk 231	0.0422	393±83	13	...	3130±156	45.0	2 ^f ,27
ESO 323-G77	0.0150	100.0±4.8	28	...	2635±132	43.1	21
IRAS 13349+2438	0.1076	1096±71	13	...	1796±90	45.0	29
IC 4329A	0.0161	178±10	4	...	6472±324	43.2	21
PGC 50427 ^e	0.0235	46.7±2.2	30	3036±74	43.1	30	7.34±0.04	-1.42
PDS 456	0.1840	1599±213	2	...	3974±764	46.3	31
PGC 89171	0.0270	303±36	4	...	2644±132	43.9	21
NGC 7603	0.0288	332±66	4	...	6350±318	44.4	21

^a This target is discussed as a changing-look quasar in the literature.

^b Mrk 590 is a changing look AGN displaying strong variability over the time of BLR and dust continuum observations (Denney et al. 2014). We do not include it in our statistical analysis.

^c The continuum radius of NGC 4151 reported by Kishimoto et al. (2011) is statistically consistent with the recent measurement from Kishimoto et al. (2022). We prefer the early measurements because it is close to the RM measurement.

^d The BLR of IRAS 09149-6206 was resolved by GRAVITY and the BH mass is derived by Gravity Collaboration et al. (2020a). The λL_λ (5100 Å) and FWHM of H β are from the BASS catalog (Koss et al. 2017).

^e The BH mass of PGC 50427 was measured by RM of the H α line (Pozo Nuñez et al. 2015). We quote the λL_λ (5100 Å) from Probst & Kollatschny (2020) observed close in time to H α RM. We measure the FWHM of H β line from the 6dF spectrum (Jones et al. 2009).

^f We converted the bolometric luminosity to λL_λ (5100 Å) using Equation (A.2) of Gravity Collaboration et al. (2020b).

^g H β FWHM is converted from H α FWHM assuming $\text{FWHM}_{H\beta}/\text{FWHM}_{H\alpha} = 1.17$ (Greene & Ho 2005).

Notes. Col. (1): Target name. Col. (2): Redshift from NASA/IPAC Extragalactic Database (NED). Col. (3): Dust continuum radius based on RM measurement. Col. (4): Reference of R_d (RM). Col. (5): Dust continuum radius based on OI measurement. Col. (6): Reference of R_d (OI). Col. (7): BLR radius based on H β time lag. Col. (8): H β FWHM. Col. (9): AGN optical luminosity at 5100 Å. Col. (10): References of R_{BLR} , FWHM, and λL_λ (5100 Å). Col. (11): BH mass derived from R_{BLR} and FWHM from Columns (7) and (8) assuming the virial factor $f = 1$. Col. (12): Eddington ratio derived from λL_λ (5100 Å) and BH mass from Columns (9) and (11) with the bolometric correction factor 9 (Peterson et al. 2004).

References: (1) Minezaki et al. (2019), (2) Gravity Collaboration et al. (2020b), (3) Du & Wang (2019), (4) GRAVITY Collaboration (in preparation), (5) Huang et al. (2019), (6) Ramolla et al. (2018), (7) Mandal et al. (2018), (8) Stalin et al. (2011), (9) Kishimoto et al. (2011), (10) Du et al. (2018), (11) Lira et al. (2011), (12) Bentz et al. (2021), (13) Kishimoto et al. (2009), (14) Sobrino Figaredo et al. (2020), (15) Lira et al. (2015), (16) Mandal et al. (2021a), (17) Barth et al. (2011), (18) Onori et al. (2017), (19) Rashed et al. (2015), (20) Gravity Collaboration et al. (2020a), (21) Koss et al. (2017), (22) Pan et al. (2021), (23) Pozo Nuñez et al. (2014), (24) Probst & Kollatschny (2020), (25) Sitko et al. (1993), (26) Shangquan et al. (2018), (27) Zheng et al. (2002), (28) Leftley et al. (2021), (29) Dong et al. (2018), (30) Pozo Nuñez et al. (2015), (31) Nardini et al. (2015).

dust continuum size of seven AGNs with $\lesssim 1$ hour observation time (GRAVITY Collaboration in preparation). We follow the method of Gravity Collaboration et al. (2020b) to measure their continuum size. To estimate the uncertainty, we sum in quadrature the statistical uncertainty of the size measurements of individual exposures and a 10% systematic uncertainty (Gravity Collaboration et al. 2020b and in preparation).

2.2. BLR measurements

The BLR size can be probed by different broad emission lines. The $H\beta$ line has been the most extensively used in RM campaigns of low- z AGNs (e.g. Bentz & Katz 2015). Meanwhile, GRAVITY spectroastrometric observations probe the BLR with $P\alpha$ and $B\gamma$ (Gravity Collaboration et al. 2018, 2020a, 2021b). Different broad lines of a BLR may show a different size due to the photoionization conditions and optical depth (Korista & Goad 2004). In this work, we only study the relation of the dust continuum radius and $H\beta$ BLR radius from the RM time lag for simplicity. Meanwhile, future GRAVITY observations measuring the BLR and dust continuum simultaneously in K -band will be powerful to investigate their relation (see Section 5). We collect the $H\beta$ BLR radii of most targets, together with their optical luminosities at 5100 \AA and $H\beta$ line FWHMs, from Table 1 of Du & Wang (2019).¹ Du & Wang (2019) averaged the quantities if there is more than one measurement. We only find a few additional AGNs from the other references (see Table 1). We adjust the λL_λ (5100 \AA) to our cosmology when necessary unless the distances of some nearby AGNs are explicitly specified in the references.

2.3. AGN variability

We emphasize that the BLR and dust continuum sizes are usually measured in different epochs. While the BLR RM campaigns of many targets conducted from 2000–2010 coincide with dust continuum RM campaigns (Koshida et al. 2014; Minezaki et al. 2019), the time difference between BLR and dust measurements for some targets can be over a decade. For example, we adopt the BLR RM of NGC 3783 measured in 2020 (Bentz et al. 2021), while its dust continuum RM was measured around 2009 (Lira et al. 2011). We find that the early BLR RM measurements of NGC 3783 (Onken & Peterson 2002) yielded a BLR radius and λL_λ (5100 \AA) quite close to the recent measurements. We, therefore, prefer to adopt the new measurements for simplicity. The asynchronous effect will contribute to the scatter of the size correlation (see discussion in Section 3).

Targets with substantial variability may show a large scatter in the $R_{\text{BLR}}-R_d$ relation. We identify so-called ‘changing-look’ AGNs in our sample from the literature and discuss them in the following. In the end, we are convinced that only Mrk 590 is not suitable to be included in our analysis. Mrk 590 transformed from a classical type 1 AGN to type 1.9–2, as its continuum luminosity decreased by 100 over the past four decades (Denney et al. 2014). The lack of evidence of intrinsic absorption indicates that changes in continuum and emission lines are due to the decline of the BH accretion rate instead of obscuration along the line of sight. The BLR of Mrk 590 was monitored through the $H\beta$ line from 1990–1996 (Peterson et al. 1998) and recently, with $H\alpha$ in 2018 (Mandal et al. 2021b). The BLR size of Mrk 590, around 25 ld, does not change significantly at the bright and faint states. The dust continuum RM campaign was conducted

from 2003 to 2007 (Koshida et al. 2014) during the rapid decline of the AGN luminosity in Mrk 590. Kokubo & Minezaki (2020) found that the dust continuum size of Mrk 590 is quite small, only ~ 33 ld, reflecting the rapid replenishment of the dust in the innermost region of the dusty interstellar medium. We exclude Mrk 590 in our statistics to avoid the complicated physics of this target. There are other changing-look AGNs in our sample, e.g. Mrk 6 and NGC 4151 (flagged in Table 1). They change either from type 1 to type 2 or vice versa (see Marin et al. 2019; Senarath et al. 2021 and references therein). However, we find the BLR and continuum were measured when they stayed the same type, so we include them in our analysis. Moreover, some changing-look AGNs flagged in our sample are likely caused by temporary changes in the line-of-sight obscuration (e.g. Goodrich 1989; Shapovalova et al. 2019). This mechanism does not relate to any intrinsic change in the AGN properties, so it will not affect the $R_{\text{BLR}}-R_d$ relation that we are interested in for this work. Nevertheless, our results stay the same if we exclude all the changing-look AGNs. Clavel et al. (1989) published their K -band RM measurement of Fairall 9 while its UV continuum flux was dropping by a factor of ~ 30 . However, an $H\beta$ RM measurement before it changed to the faint state does not exist. The extreme variability, from type 1 to almost type 2 (Kollatschny & Fricke 1985; Lub & de Ruiter 1992), prevents a simple choice of λL_λ (5100 \AA) and $H\beta$ FWHM for our analysis. Therefore, we chose to exclude Fairall 9 in this work.

3. Scaling relations of BLR and dust continuum size

Figure 1 displays our sample. The dust $R-L$ relations measured by both RM and OI are systematically above the BLR $R-L$ relation. Moreover, the continuum size measured by OI is above that of RM. The $R-L$ relations of dust RM and OI measurements have been discussed in many previous works (e.g. Suganuma et al. 2006; Kishimoto et al. 2009, 2011; Koshida et al. 2014; Minezaki et al. 2019; Gravity Collaboration et al. 2020b). One common explanation is that the RM-measured time lag is weighted by the amplitude of flux variations, which is expected to originate most strongly from the inner boundary of the hot dust; on the other hand, OI-measured sizes are mainly flux-weighted and, therefore, are elevated by contributions of lower temperature dust at larger radii (Kishimoto et al. 2009, 2011). Another slightly different explanation assumes that the dust structure is a ‘bowl shape’ (Kawaguchi & Mori 2010): we mainly observe the foreground side at a low inclination angle for type 1 AGNs, and dust at larger radii is also closer to the observer, so the projected size increases more significantly than their RM time lag towards larger radii (Pozo Nuñez et al. 2014; Sobrino Figaredo et al. 2020). A more detailed discussion of BLR and dust structure models is beyond the scope of this paper. Throughout the paper, we use OI and RM to refer to the dust continuum measurements from these two different methods unless otherwise clarified.

Previous works studying both RM and OI observations have hinted that the slope of the dust continuum $R-L$ relation is shallower than $\propto L^{0.5}$. The slopes in our current RM and OI samples are both about 0.4, consistent with previous works. We leave a more detailed discussion of the $R-L$ relation in a separate paper (GRAVITY Collaboration et al. in preparation). In summary, previous RM studies provide various explanations of the shallower slope relating to the dust structure, dust response to the accretion disk emission, and its putative effect on the observed optical luminosity (e.g. Minezaki et al. 2019; Sobrino Figaredo et al. 2020). Based on the OI measurements, Gravity Collabora-

¹ Similar data are also collected in Dalla Bontà et al. (2020).

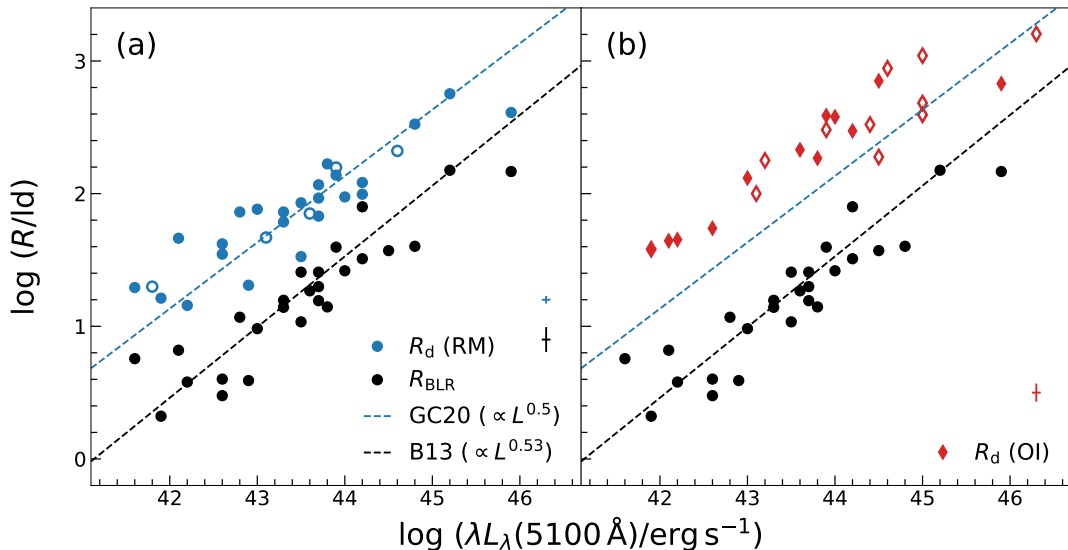


Fig. 1. Size–luminosity relations of the dust continuum measured by (a) RM (blue circles) and (b) OI (red diamonds) are systematically above that of the BLR (black circles; same in both panels). The open-colored circles indicate sources without BLR measurements. The dashed lines in both panels are based on RM-measured R – L relations of the dust continuum (blue; [Gravity Collaboration et al. 2020b](#)) and the BLR (black; [Bentz et al. 2013](#)). The typical uncertainties are shown on the lower right of each panel.

[tion et al. \(2020b\)](#) suspect the continuum emission of the accretion disk may bias the OI size measurement for the most luminous sources.

Likewise, recent RM BLR measurements ([Du et al. 2015](#); [Grier et al. 2017](#)) also find targets with R_{BLR} significantly lower than the canonical BLR R – L relation (e.g. [Bentz et al. 2013](#)). Some works find that the deviation closely correlates with the accretion rate of the BH ([Du et al. 2015](#); [Du & Wang 2019](#); [Martínez-Aldama et al. 2019](#); [Dalla Bontà et al. 2020](#)), while the physical driver remains unclear in some other works ([Grier et al. 2017](#); [Fonseca Alvarez et al. 2020](#)). The physical explanation of the deviation of BLR and dust continuum R – L relations is beyond the scope of the current paper. As discussed in the following sections, we find tight relations between R_{BLR} and R_{d} , which are close to linear, reflecting a simple link between the two physical structures.

3.1. Statistical analysis

We find strong correlations between BLR and dust continuum sizes, as shown in Figure 2. We fit the relations for RM- and OI-measured R_{d} separately as they show systematic differences. We fit the data with a power-law relation,

$$\log(R_{\text{BLR}}/l_{\text{d}}) = \alpha + \beta \log(R_{\text{d}}/R_{\text{d},0}), \quad (2)$$

where α and β are the intercept and the slope, and $R_{\text{d},0}$ is a pivot point fixed close to the median of R_{d} of the data to reduce the degeneracy of α and β . We adopt the Bayesian Markov Chain Monte Carlo (MCMC) approach to fit the data. The likelihood is,

$$\ln \mathcal{L} = -\frac{1}{2} \sum_i \left(\ln(2\pi\sigma_i^2) + \frac{(y_i - m_i)^2}{\sigma_i^2} \right), \quad (3)$$

where y_i is $\log R_{\text{BLR}}$ data, m_i is the model value based on $\log R_{\text{d}}$ and Equation (2), and $\sigma_i^2 = (\beta\sigma_{x,i})^2 + \sigma_{y,i}^2 + \epsilon^2$ includes the measurement uncertainties of the dust continuum ($\sigma_{x,i}$) and BLR ($\sigma_{y,i}$) radius as well as the intrinsic scatter (ϵ). We adopt uniform priors of the parameters that are wide enough and sample

Table 2. Best-fit parameters of Equation (2)

Relation	α	β	ϵ	$\log(R_{\text{d},0}/l_{\text{d}})$
RM (free)	$1.20^{+0.05}_{-0.05}$	$1.12^{+0.13}_{-0.13}$	$0.21^{+0.05}_{-0.04}$	1.9
OI (free)	$1.19^{+0.08}_{-0.08}$	$1.10^{+0.18}_{-0.18}$	$0.25^{+0.08}_{-0.06}$	2.2
RM (fixed)	$1.20^{+0.05}_{-0.05}$	1	$0.21^{+0.04}_{-0.04}$	1.9
OI (fixed)	$1.19^{+0.08}_{-0.08}$	1	$0.24^{+0.07}_{-0.05}$	2.2

Notes. We fit the R_{BLR} – R_{d} relation for AGNs with R_{d} measured by RM and OI, respectively. α , β , and ϵ are the intercept, slope, and intrinsic scatter of a linear relation. $R_{\text{d},0}$ is the pivot point fixed in the fitting. The first two rows provides the best-fit parameters with β free, while the last two rows are results with β fixed to unity. OI-measured R_{d} is about 0.3 dex larger than that measured by the RM.

the posterior with the widely used Python package of MCMC, emcee ([Foreman-Mackey et al. 2013](#)). We used 32 walkers and 5000 steps, with the first 500 steps discarded as burn-in steps. The fitting is well converged.

The best-fit relations are very close to linear (throughout the paper, ‘linear’ refers $\beta = 1$) when we allow the slope to be free, as shown in Figure 2a. Therefore, we also fit the data with the slope fixed to unity (Figure 2b). The best-fit results are listed in Table 2. For simplicity, we will take the β -fixed fitting results in the following discussion and derive the BLR radius and BH mass with R_{d} in Section 4. Given current uncertainties, whether we adopt the relations with β free or fixed does not affect these results.

The dust continuum size measured from RM is about 0.7 dex (five times) larger than the BLR size, which is consistent with previous works (e.g. [Koshida et al. 2014](#); [Kokubo & Minezaki 2020](#)). The dust continuum size measured by OI is about 0.3 dex (two times) larger than that measured by RM, again consistent with previous studies ([Kishimoto et al. 2011](#); [Koshida et al. 2014](#); [Gravity Collaboration et al. 2020b](#)). We do not find the slope of the R_{BLR} – R_{d} relation to significantly deviate from unity. However, for the relation to be linear, any departure from $\propto L^{0.5}$

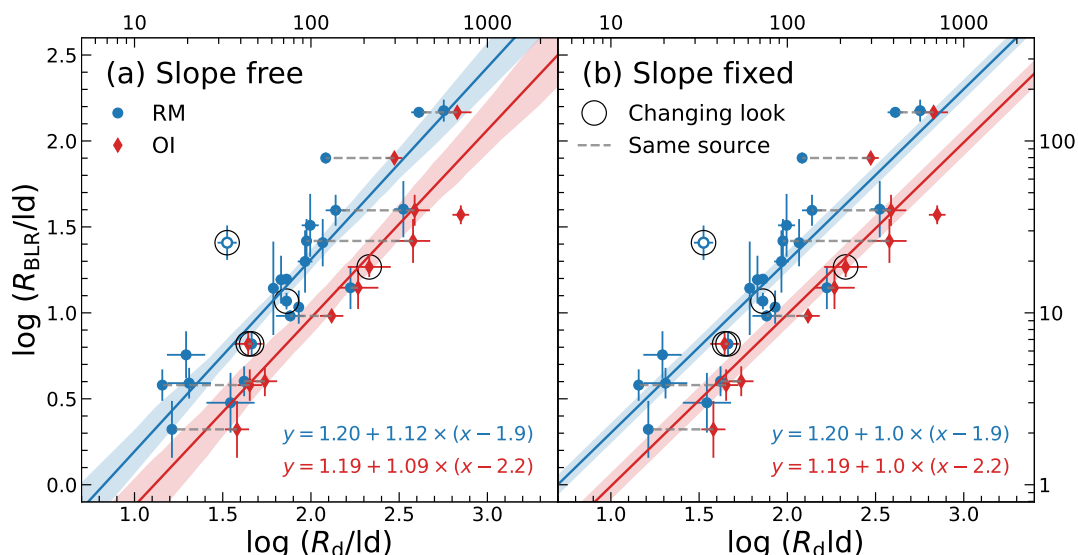


Fig. 2. Tight relations between the radii of the BLR and the dust continuum. The blue circles are AGNs measured by RM, and the red diamonds are the targets measured by OI. The gray dashed lines connect the same sources with both RM and OI measured R_d . The best-fit $R_{\text{BLR}}-R_d$ relations of RM and OI datasets (formula in the lower right corner of each panel) are shown as the blue and red lines, respectively. The black circles enclose the known changing-look AGNs. We only exclude Mrk 590, denoted as the empty blue circle, in our analysis. The best-fit results with the slope free (a) or fixed to unity (b) are almost the same, so we mainly adopt the results of (b) in the discussion. The linear scale is indicated on the top and right axes.

for the $R-L$ relations of the dust continuum and the BLR must be similar. Our sample shows a more significant deviation in $R_d-\lambda L_\lambda$ (5100 Å) than that in $R_{\text{BLR}}-\lambda L_\lambda$ (5100 Å). This difference may contribute to the scatter of the $R_{\text{BLR}}-R_d$ relation, which we will discuss in Section 3.3.

3.2. Intrinsic scatter

The intrinsic scatter of the best-fit relations is about 0.25 dex for both RM and OI relations. The physical difference between the BLR and dust structure for individual targets may contribute to the scatter. Such a variation was observed in the mid-IR, where a large scatter of the $R-L$ relation was observed (Burtcher et al. 2013). However, besides the individual BLR and dust structure difference, for the $R-L$ relation, the uncertainty of the bolometric luminosity of an AGN is another primary source of the scatter. Studying the BLR and dust structure with the $R_{\text{BLR}}-R_d$ relation allows us to avoid the uncertain bolometric luminosity. However, AGN variability still likely introduces considerable intrinsic scatter because the BLR and dust continuum sizes are not measured in a state where they reflect the same AGN bolometric luminosity.

As described in Section 2.3, most of the dust continuum RM measurements are made between 2001 and 2008, while the OI measurements are around 2009–2010 (Keck interferometry) and 2018–2022 (GRAVITY). The BLR measurements are conducted from the 1980s until recent years. NGC 5548 is one of the best targets to investigate the variability: Du & Wang (2019) collected 18 epochs of its BLR RM measurements from 1989 to 2015, and the BLR radius (time lag) varies from 4.2 l_d to 26.5 l_d with a standard deviation of 0.24 dex. Mrk 335 and Mrk 817 also have four epochs of BLR measurements across > 10 years, and their BLR radii changes are $\gtrsim 0.3$ dex. For the dust continuum, Koshida et al. (2014) reported 6 epochs of dust continuum RM measurements for NGC 5548 from 2001 to 2007; the RMS of the dust continuum radius is about 0.1 dex. Other AGNs,

NGC 3227, NGC 4051, and NGC 4151, with ≥ 4 epochs of dust RM measurements, also show similar ~ 0.1 dex RMS variation. NGC 3783 was observed from 1974–1990 (Glass 1992) and later in 2006–2009 (Lira et al. 2011); the measured K -band time lags are consistent within their uncertainties. It is not surprising that the dust continuum size shows less variability: the dust re-radiation effectively averages the variability of the central engine on a longer time scale, while the RM technique measures the averaged size over the monitoring period.

Since the BLR size variation of the AGNs with multiple measurements always reach $\gtrsim 0.2$ dex, we conclude that the observed 0.25 dex intrinsic scatter of the $R_{\text{BLR}}-R_d$ relations can be explained by the time variation of the BLR and dust continuum sizes, while the physical difference between the BLR and dust structures of individual targets also plays a role. Future simultaneous measurements of BLR and dust continuum sizes have the potential to reveal a tighter $R_{\text{BLR}}-R_d$ relation, while the related caveats are discussed in Section 4.3.

3.3. Higher-order correlations

We investigate whether the scatter of the $R_{\text{BLR}}-R_d$ relation correlates with the physical properties of the AGN. Since the $R_{\text{BLR}}-R_d$ relations are remarkably close to linear (Section 3.1), we study the dependence of the ratio, R_{BLR}/R_d , on the other physical parameters of the AGN. We calculate Spearman’s rank correlation coefficients to test the significance of the correlations. We perturb R_{BLR}/R_d 500 times with the measurement uncertainties of R_{BLR} and R_d to calculate the p -value distribution. The resulting p -values do not support any significant correlations (i.e. $p > 0.05$). We find that the conclusions do not change when we study the deviation of the $R_{\text{BLR}}-R_d$ relations from the best-fit results with β free.

We first investigate R_{BLR}/R_d against the AGN luminosity and the Eddington ratio (Figure 3). Although the p -values do not support significant correlations, we notice that, at λL_λ (5100 Å) >

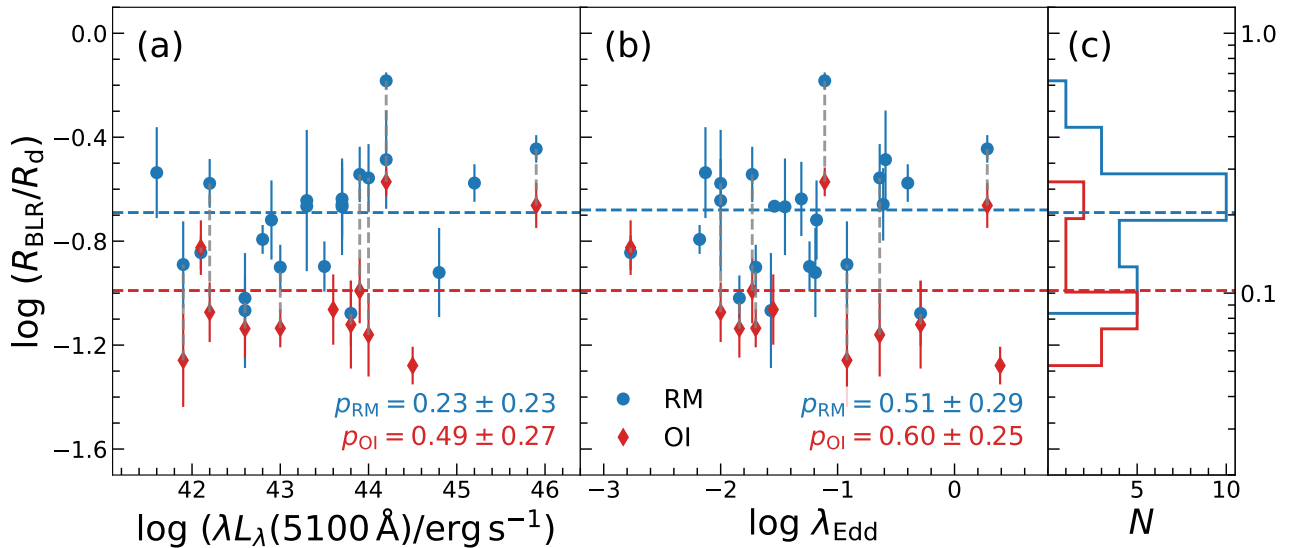


Fig. 3. Ratio of BLR and dust continuum sizes as a function of (a) the AGN luminosity and (b) the Eddington ratio. The p -values of Spearman’s rank correlation coefficient are reported in the lower right corner of each panel for RM- and OI-measured samples. The notations are the same as in Figure 2. The error bars are the quadrature sum of the uncertainties of R_{BLR} and R_{d} . Panel (c) displays the histograms of the ratios. The dashed lines indicate the averaged $R_{\text{BLR}}/R_{\text{d}}$ based on the fitting of the $R_{\text{BLR}}-R_{\text{d}}$ relations with β fixed to unity (see also Equation (4)). $R_{\text{BLR}}/R_{\text{d}}$ does not show a statistically significant correlation with the $\lambda L_{\lambda}(5100 \text{ \AA})$ nor the Eddington ratio. The linear scale of $R_{\text{BLR}}/R_{\text{d}}$ is indicated on the right.

$10^{45} \text{ erg s}^{-1}$, the three data points of PG 0953+414 and 3C 273 are all above the averaged values of $R_{\text{BLR}}/R_{\text{d}}$. This trend may drive the slope to values slightly larger than 1 when we fit the $R_{\text{BLR}}-R_{\text{d}}$ relation with the slope free. Unfortunately, our current sample has too few luminous AGNs to confirm such a trend. Previous BLR RM studies have found that the Eddington ratio may drive the deviation of the $R-L$ relation such that highly accreting AGNs display shorter time lags (e.g. Du et al. 2015). We do not find a dependence of $R_{\text{BLR}}/R_{\text{d}}$ on the Eddington ratio. Nevertheless, our targets do not show significant deviation from the Bentz et al. (2013) relation either (Figure 1). It is worth noting that Mrk 509, which displays the highest deviation of $R_{\text{BLR}}/R_{\text{d}}$ has only $\lambda L_{\lambda}(5100 \text{ \AA}) \approx 10^{44.2} \text{ erg s}^{-1}$ and intermediate Eddington ratio. More observations are needed to understand the details of the $R_{\text{BLR}}-R_{\text{d}}$ relation.

We further investigate the dependence of $R_{\text{BLR}}/R_{\text{d}}$ on R_{d} , R_{BLR} , and the FWHM of H β (Figure 4). Again, Spearman’s rank correlation coefficients do not support a significant correlation with any of the three parameters. We only find a tentative trend that all three targets, PG 0953+414, 3C 373, and Mrk 509, with $R_{\text{BLR}} \gtrsim 50 \text{ ld}$ in Figure 4b show $R_{\text{BLR}}/R_{\text{d}}$ above the averaged values. This trend is similar to what is discussed above for $\lambda L_{\lambda}(5100 \text{ \AA}) > 10^{45} \text{ erg s}^{-1}$ AGNs, although we caution that the intrinsic scatter of the $R_{\text{BLR}}-R_{\text{d}}$ relation will naturally lead to the correlation between $R_{\text{BLR}}/R_{\text{d}}$ and R_{BLR} .

Moreover, in our sample, AGNs with the largest radii are at $z \gtrsim 0.1$. Their K -band measurements probe continuum emission at a slightly shorter wavelength ($\lesssim 2 \mu\text{m}$) than the rest of the sample. One may simply expect the continuum size to be smaller at shorter wavelengths because of a larger contribution from higher temperature dust that is closer to the central engine (e.g., Oknyansky et al. 2015). Indeed, a sharp decrease in the time lag towards shorter wavelength was observed for NGC 4151 (Oknyanskij et al. 1999) and GQ Com (Sitko et al. 1993). However, it is more common that the time lags of dust emission only decrease moderately towards shorter wavelength (Oknyansky et al. 2015). A bi-conical dust distribution can explain this

because dust with different temperatures is located on similar isodelay surfaces. Therefore, we suggest that the redshift effect is not likely to cause the observed deviation. However, it is hard to draw a firm conclusion with the limited number of measurements. More observations of AGNs with high luminosity and/or at high redshift would be essential to investigate this problem further.

4. Estimating BH masses with dust continuum sizes

4.1. BLR radius based on dust continuum measurements

We can now use the measured dust continuum radius to estimate the BLR radius for AGNs lacking BLR measurements. We adopt the best-fit parameters with $\beta = 1$ in Table 2 so that Equation (2) can be written as

$$\log R_{\text{BLR}} = \begin{cases} \log R_{\text{d}} - 0.70 & (\text{RM}), \\ \log R_{\text{d}} - 1.01 & (\text{OI}). \end{cases} \quad (4)$$

We adopt 0.25 dex as the uncertainty of R_{BLR} based on the intrinsic scatter of the $R_{\text{BLR}}-R_{\text{d}}$ relation. We expect the uncertainty of the $R_{\text{BLR}}-R_{\text{d}}$ relations to be reduced in the future with more observations of the BLR and continuum close in time and of more luminous AGNs with large BLR sizes (however, see Section 4.3).

In Table 3, we report the R_{BLR} derived from Equation (4) for AGNs in the lower part of Table 1. We plot these targets in Figure 5 with their R_{BLR} against $\lambda L_{\lambda}(5100 \text{ \AA})$. The continuum-based R_{BLR} follows the $R-L$ relation of the direct BLR measurements. Similar to Du & Wang (2019) and Grier et al. (2017)’s results, we find AGNs more likely below the Bentz et al. (2013) relation, especially for the luminous ($\lambda L_{\lambda}(5100 \text{ \AA}) > 10^{44} \text{ erg s}^{-1}$) objects. Although we are still limited by the small number of objects, the distribution of our targets closely resembles the RM measured sample. Four targets, Mrk 1239, Mrk 231, IRAS 09149–6206, and PDS 456, show the most significant deviation from the Bentz et al. (2013) relation. As discussed in

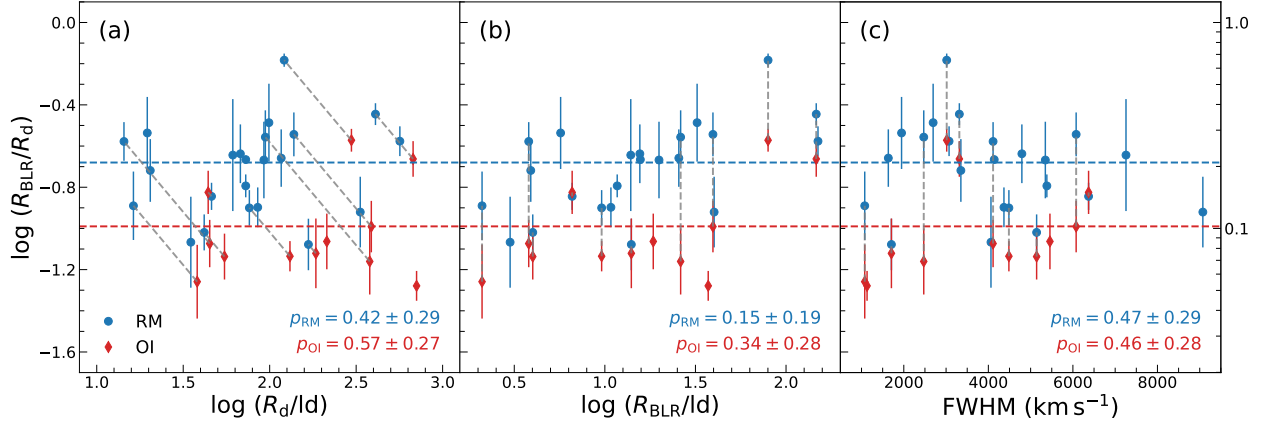


Fig. 4. Ratio of R_{BLR} and R_d as a function of (a) the continuum radius, (b) the BLR radius, and (c) the FWHM of $\text{H}\beta$ line. We do not find any statistically significant correlation. However, all of the AGNs with $R_{\text{BLR}} \geq 50$ ld show R_{BLR}/R_d above the averaged values. We discuss this tentative trend in the text. The notations are the same as in Figure 3. The linear scale of R_{BLR}/R_d is indicated on the right.

Table 3. BH mass and Eddington ratio derived with dust continuum size

Name	$\log R_{\text{BLR}}$ (ld)	$\log M_{\text{BH}}$ (M_{\odot})	$\log \lambda_{\text{Edd}}$
(1)	(2)	(3)	(4)
NGC 1365	0.57 ± 0.26	6.26	-1.51
IRAS 03450+0055	1.50 ± 0.25	7.77	-1.02
IRAS 09149-6206	1.67 ± 0.25	8.23	-0.37
Mrk 1239	1.27 ± 0.26	6.40	0.96
WPVS 48	1.15 ± 0.25	6.99	-0.54
HE 1029-1401	1.93 ± 0.26	8.73	-1.28
Mrk 744	0.60 ± 0.25	7.39	-2.73
GQ Com	1.62 ± 0.26	8.32	-0.86
Mrk 231	1.58 ± 0.27	7.87	-0.01
ESO 323-G77	0.99 ± 0.25	7.12	-1.17
IRAS 13349+2438	2.03 ± 0.25	7.83	0.02
IC 4329A	1.24 ± 0.25	8.17	-2.10
PGC 50427	0.97 ± 0.25	7.22	-1.27
PDS 456	2.19 ± 0.26	8.68	0.47
PGC 89171	1.47 ± 0.26	7.61	-0.85
NGC 7603	1.51 ± 0.26	8.41	-1.15

Notes. Col. (1): Target name. Col. (2): BLR radius derived from R_d with Equation (4). However, we find the difference between the results using the best-fit relations with β fixed and free is much smaller than the uncertainties. Col. (3): BH mass derived from R_{BLR} and $\text{H}\beta$ FWHM assuming the virial factor $f = 1$. Col. (4): Eddington ratio derived from λL_{λ} (5100 Å) (Col. (9) of Table 1) and BH mass from Col. (3).

Section 4.2, all of them, except for IRAS 09149-6206, are at or above or above their Eddington luminosity. The Eddington ratio of IRAS 09149-6206 (about 0.4) is also high among the typical AGNs (e.g. the rest of the sample). Thus the large deviations from the R - L relation could be related to their high accretion rates (Du & Wang 2019).

4.2. BH mass

Since our continuum-based R_{BLR} is fully consistent with RM-measured R_{BLR} , one can simply adopt Equation (1) and the virial factor previously calibrated for the RM method to derive the BH mass. We adopt $f = 1$ to be consistent with Du

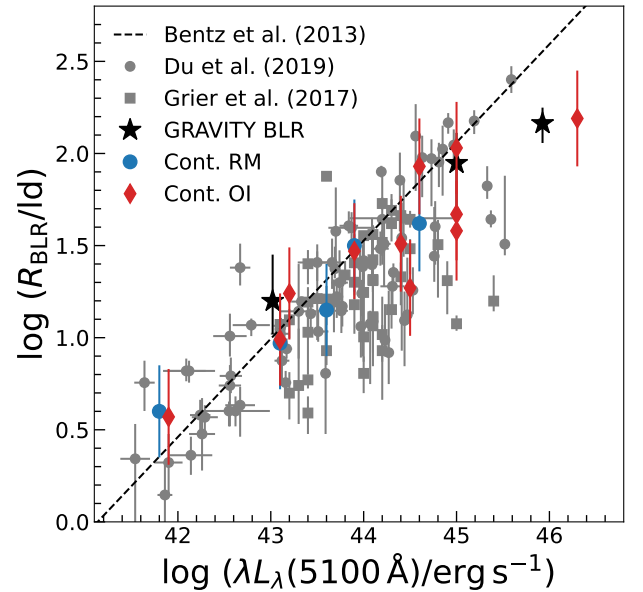


Fig. 5. BLR R - L relation of AGNs measured by the continuum-based method. The blue circles and red diamonds are dust radii measured by RM and OI, respectively. The black stars are three AGNs whose BLR kinematics are resolved by GRAVITY (Gravity Collaboration et al. 2018, 2020a, 2021b). The gray circles and squares are BLR RM measured AGNs from Du & Wang (2019) and Grier et al. (2017) respectively. The dashed line is the best-fit R - L relation from Bentz et al. (2013). The continuum-based method derives the BLR radii following a similar trend of the R - L relation based on RM and GRAVITY BLR measurements.

& Wang (2019). The FWHM of the $\text{H}\beta$ line can be obtained from a single-epoch spectrum (Table 1). We further calculate the Eddington ratios of these targets with the bolometric luminosities scaled from λL_{λ} (5100 Å) by a bolometric correction factor of 9 (Peterson et al. 2004). Four AGNs, Mrk 1239, Mrk 231, IRAS 13349+2438, and PDS 456, are close to or above the Eddington accretion. Their optical spectra (see their references in Col. (10) of Table 1) commonly show features of narrow widths of the broad $\text{H}\beta$ lines, weak or no $[\text{O III}] \lambda\lambda 4959, 5007$ lines, and strong Fe II features. These features strongly indicate that these targets have high accretion rates (Boroson & Green 1992; Shen & Ho 2014 and references therein), consistent with our Edding-

ton ratios. The BH masses of IRAS 09149–6206 and PGC 50427 are $10^{8.06} M_{\odot}$ and $10^{7.34} M_{\odot}$, based on the spectroastrometry of the broad Br γ line (Gravity Collaboration et al. (2020a)) and the RM of H α line (Poza Nuñez et al. 2015), respectively. Our derived BH masses by the continuum-based method are very close (< 0.2 dex) to those from the direct BLR measurements.

The primary uncertainty of the RM method to measure the BH mass comes from the virial factor. The calibration of f typically shows ~ 0.4 dex intrinsic scatter (Woo et al. 2010; Ho & Kim 2014), which consists of the variation of the BLR structure of individual targets and the intrinsic scatter of the $M_{\text{BH}}-\sigma_*$ relation (Gebhardt et al. 2000; Ferrarese & Merritt 2000). The sample selection and regression method may introduce a factor of 2 systematic difference of the virial factor (Graham et al. 2011; Park et al. 2012). The virial factor may differ by a factor of 2 depending on the bulge type (classical bulge and pseudo bulge; Ho & Kim 2014), which might be correlated to the systematics of the sample selection. For individual AGNs, one way to measure their virial factors is via dynamically modeling the velocity-resolved RM data (Pancoast et al. 2014a,b). Based on dynamical modeling results, Williams et al. (2018) find 0.2–0.5 dex uncertainties on the predictive distribution of the virial factor corresponding to different definitions of the line width. One should be cautious that the small scatter (e.g. 0.2 dex) may be due to the narrow range of parameter space spanned by their small sample. Altogether, to derive the BH mass, the uncertainty of the virial factor is likely ≥ 0.3 dex. Since the continuum-based method shares the same uncertainty of the virial factor as the RM method, the $R_{\text{BLR}}-R_{\text{d}}$ relation provides a promising method to measure the BH mass close, if not equivalent, to the accuracy of the RM method.

The single-epoch method is generally believed to be much more uncertain than RM due to the intrinsic scatter and the systematic bias of the $R-L$ relation. The systematic deviation of the measured R_{BLR} from the canonical $R-L$ relation is discussed in Section 3 and Section 4.1. Dalla Bontà et al. (2020) recently provided the state-of-the-art calibration of the single-epoch method with the RM database (Bentz & Katz 2015) and SDSS RM (Grier et al. 2017) samples. Their calibration empirically includes the secondary dependence of the Eddington ratio which results in an intrinsic scatter of 0.31 dex for the virial product ($\propto R_{\text{BLR}}\Delta V^2$) when the line dispersion (in contrast to the FWHM) is used. This scatter is equivalent to the intrinsic scatter we find for the $R_{\text{BLR}}-R_{\text{d}}$ relation ($\lesssim 0.25$ dex) which will be the main contributor to the continuum-based virial product. We expect the continuum-based method scatter can be reduced with future observations of the BLR and the dust continuum size close in time, but we discuss the caveats in Section 4.3. We believe the direct dust continuum size measurement, which we have shown is tightly linked to the BLR size, is promising to provide high-accuracy BH masses in the future (more discussion in Section 5).

4.3. Caveats

The primary goal of this work is to propose the idea of measuring the BH mass based on the dust continuum size, particularly with time-efficient OI observations. The current calibration is not ideal because the BLR and dust continuum are not measured in the same AGN luminosity state. The line width measurements in the lower part of Table 1 are collected from different epochs too. This may introduce significant uncertainty on the BH mass (Table 3), because the latter is $\propto \Delta V^2$. Due to this reason, we caution that the BH mass and Eddington ratio in Table 3 are only for the

purpose to discuss the new method instead of rigorous measurements.

In practice, it may not be easy to measure the BLR and dust continuum size when they reflect the same luminosity state in order to calibrate the $R_{\text{BLR}}-R_{\text{d}}$ relation. It is more feasible to measure the BLR and the dust continuum sizes close in time (see also Section 5). In this way, the different time lags of the BLR and the hot dust will contribute to the intrinsic scatter of their size relation. The BLR size and the line width may show quicker and stronger variations than the dust continuum because the BLR has 5–10 times smaller size than the dust continuum. We expect a stronger averaging effect on the dust continuum too. For an extreme example, the dust continuum size may be correlated with a long-term average of the AGN luminosity over the previous several years, as discussed by Kishimoto et al. (2013) for NGC 4151. Future observations are important to quantify how much we can improve the $R_{\text{BLR}}-R_{\text{d}}$ relation from the first calibration provided in this work.

The current calibration of the $R_{\text{BLR}}-R_{\text{d}}$ relation is limited by the sample size. As briefly discussed in Section 3, various physical mechanisms may lead to the deviation of $R \propto L^{0.5}$ for both the BLR and the hot dust. Such deviations may reflect variations of BLR and hot dust structures, which may not necessarily follow each other. For example, the BLR radius may have a secondary dependence on the BH accretion rate (Du et al. 2015; Du & Wang 2019), while the dust sublimation radius does not depend on it (Barvainis 1987; Kishimoto et al. 2007). This difference means that the $R_{\text{BLR}}-R_{\text{d}}$ relation may depend on some secondary physical parameters, such as the accretion rate. Such a dependence is not found in the current sample (Section 3.3), but we cannot rule out the possibility that we are limited by the parameter space of the current sample. Following Du et al. (2015, Equation 2), we calculate the dimensionless accretion rate, \dot{M} and find that our targets span $10^{-3} \lesssim \dot{M} \lesssim 200$, with 23% of our targets falling in their super-Eddington regime ($\dot{M} > 3$). We do not find a correlation between $R_{\text{BLR}}/R_{\text{d}}$ and \dot{M} , but this correlation is worth revisiting with future larger samples including more high accretion rate AGNs.

5. Prospects

OI observations have great potential to measure the BLR and continuum of AGNs in the future. Current GRAVITY observations are limited to the brightest targets ($K < 11$). With the ongoing upgrade to significantly improve its sensitivity and sky coverage, GRAVITY+ will be capable of observing $K < 13$ AGNs in on-axis mode or even fainter AGNs in off-axis mode with a phase reference source at $\lesssim 30''$ (GRAVITY+ Collaboration et al. 2022), enabling observations of thousands of AGNs from $z \lesssim 0.2$ out to $z \gtrsim 2$.

Dust continuum sizes are a side product of GRAVITY(+) spectroastrometry observations of the BLR if the AGN itself is bright enough to be the phase reference. Half of the AGN emission is split into the low-resolution beam combiner (or the ‘fringe tracker’), which is used as the phase reference of the long-time exposure in the science channel to measure the BLR spectroastrometric signal (Gravity Collaboration et al. 2017). The dust continuum size can be measured from the visibility of the fringe tracker data. Since the spectroastrometric measurement constrains the BLR geometry and dynamics and the BH mass for individual AGNs, we can use the simultaneous measurements of the BLR and continuum to calibrate the virial factor in Equation (1) directly for R_{d} instead of R_{BLR} . This approach will fur-

ther improve the accuracy of BH masses from the continuum-based method.

GRAVITY can efficiently measure the dust continuum size, e.g. $\lesssim 1$ hour observation for one source with current sensitivity (GRAVITY Collaboration et al. in preparation). We can put all AGN light into the fringe tracker so that the continuum method can measure the BH mass of AGNs a factor of two (or 0.75 mag) fainter than the spectroastrometry method. GRAVITY+ observations will be able to measure the dust continuum size and derive the BLR size of a few hundreds of $z \lesssim 0.2$ AGNs, including many sources with $\lambda L_{\lambda}(5100 \text{ \AA}) > 10^{45} \text{ erg s}^{-1}$. They will be crucial to understanding the dependence of BLR properties and the BH accretion on the AGN properties.

6. Summary

In this paper, we collect 42 AGNs with dust continuum size measurements from RM and/or OI observations. Among them, the BLR size based on $H\beta$ RM measurements of 26 AGNs are available. We find close linear relations between the BLR and dust continuum radius with an intrinsic scatter of only 0.25 dex. The dust continuum radius measured by OI is about twice as large as that measured by RM. Dust continuum radii measured by RM and OI are about five and ten times the radius of the BLR, respectively. We provide simple scaling relations to derive the BLR radius based on the dust continuum radius, measured with RM and OI separately. For the remaining 16 AGNs, we calculate their BLR radii, BH masses, and Eddington ratios using the $R_{\text{BLR}}-R_{\text{d}}$ relations. We find that these AGNs consistently follow the BLR $R-L$ relation of previous RM and GRAVITY measurements. All targets significantly below the Bentz et al. (2013) relation show a high Eddington ratio.

The accuracy of the continuum-based BH mass is comparable to that of the integrated broad emission line RM measurements since the primary uncertainty comes from the virial factor. The primary goal of this paper is to propose a new method to measure the BH mass based on the dust continuum size. We discuss the caveats of the method in detail. More continuum observations close in time with BLR measurements will be essential to study better the $R_{\text{BLR}}-R_{\text{d}}$ relation in the future. In particular, it is important to test whether luminous AGNs with large BLRs show a different $R_{\text{BLR}}-R_{\text{d}}$ relation compared to their low-luminosity counterparts. With its improved sensitivity, GRAVITY+ will be powerful to improve the continuum-based method and to efficiently measure the BH mass for a large sample of AGNs in the low-redshift Universe using this method.

Acknowledgements. We thank the anonymous referees for their careful reading and suggestions that helped to improve this manuscript. This research has made use of the NASA/IPAC Extragalactic Database (NED) which is operated by the California Institute of Technology, under contract with the National Aeronautics and Space Administration. This research has made use of the SIMBAD database, operated at CDS, Strasbourg, France.

References

Baribaud, T., Alloin, D., Glass, I., & Pelat, D. 1992, A&A, 256, 375
 Barth, A. J., Nguyen, M. L., Malkan, M. A., et al. 2011, ApJ, 732, 121
 Barvainis, R. 1987, ApJ, 320, 537
 Baskin, A. & Laor, A. 2018, MNRAS, 474, 1970
 Bentz, M. C., Denney, K. D., Grier, C. J., et al. 2013, ApJ, 767, 149
 Bentz, M. C. & Katz, S. 2015, PASP, 127, 67
 Bentz, M. C., Street, R., Onken, C. A., & Valluri, M. 2021, ApJ, 906, 50
 Blandford, R. D. & McKee, C. F. 1982, ApJ, 255, 419
 Boizelle, B. D., Barth, A. J., Walsh, J. L., et al. 2019, ApJ, 881, 10
 Boroson, T. A. & Green, R. F. 1992, ApJS, 80, 109

Burtscher, L., Meisenheimer, K., Tristram, K. R. W., et al. 2013, A&A, 558, A149
 Clavel, J., Wamsteker, W., & Glass, I. S. 1989, ApJ, 337, 236
 Collin, S., Kawaguchi, T., Peterson, B. M., & Vestergaard, M. 2006, A&A, 456, 75
 Dalla Bontà, E., Peterson, B. M., Bentz, M. C., et al. 2020, ApJ, 903, 112
 Davis, T. A. 2014, MNRAS, 443, 911
 Denney, K. D., De Rosa, G., Croxall, K., et al. 2014, ApJ, 796, 134
 Dong, X. Y., Wu, X.-B., Ai, Y. L., et al. 2018, AJ, 155, 189
 Du, P., Brotherton, M. S., Wang, K., et al. 2018, ApJ, 869, 142
 Du, P., Hu, C., Lu, K.-X., et al. 2015, ApJ, 806, 22
 Du, P. & Wang, J.-M. 2019, ApJ, 886, 42
 Ferrarese, L. & Merritt, D. 2000, ApJ, 539, L9
 Fonseca Alvarez, G., Trump, J. R., Homayouni, Y., et al. 2020, ApJ, 899, 73
 Foreman-Mackey, D., Hogg, D. W., Lang, D., & Goodman, J. 2013, PASP, 125, 306
 Gebhardt, K., Bender, R., Bower, G., et al. 2000, ApJ, 539, L13
 Glass, I. S. 1992, MNRAS, 256, 23P
 Goodrich, R. W. 1989, ApJ, 340, 190
 Graham, A. W., Onken, C. A., Athanassoula, E., & Combes, F. 2011, MNRAS, 412, 2211
 Gravity Collaboration, Abuter, R., Accardo, M., et al. 2017, A&A, 602, A94
 GRAVITY+ Collaboration, Abuter, R., Allouche, F., et al. 2022, arXiv e-prints, arXiv:2206.00684
 Gravity Collaboration, Amorim, A., Bauböck, M., et al. 2021a, A&A, 654, A85
 Gravity Collaboration, Amorim, A., Bauböck, M., et al. 2021b, A&A, 648, A117
 Gravity Collaboration, Amorim, A., Bauböck, M., et al. 2020a, A&A, 643, A154
 Gravity Collaboration, Dexter, J., Shangguan, J., et al. 2020b, A&A, 635, A92
 Gravity Collaboration, Sturm, E., Dexter, J., et al. 2018, Nature, 563, 657
 Greene, J. E. & Ho, L. C. 2005, ApJ, 630, 122
 Grier, C. J., Martini, P., Watson, L. C., et al. 2013, ApJ, 773, 90
 Grier, C. J., Trump, J. R., Shen, Y., et al. 2017, ApJ, 851, 21
 Hicks, E. K. S. & Malkan, M. A. 2008, ApJS, 174, 31
 Ho, L. C. & Kim, M. 2014, ApJ, 789, 17
 Huang, Y.-K., Hu, C., Zhao, Y.-L., et al. 2019, ApJ, 876, 102
 Jones, D. H., Read, M. A., Saunders, W., et al. 2009, MNRAS, 399, 683
 Kaspi, S., Smith, P. S., Netzer, H., et al. 2000, ApJ, 533, 631
 Kawaguchi, T. & Mori, M. 2010, ApJ, 724, L183
 Kishimoto, M., Anderson, M., ten Brummelaar, T., et al. 2022, arXiv e-prints, arXiv:2209.06061
 Kishimoto, M., Höning, S. F., Antonucci, R., et al. 2011, A&A, 527, A121
 Kishimoto, M., Höning, S. F., Antonucci, R., et al. 2009, A&A, 507, L57
 Kishimoto, M., Höning, S. F., Antonucci, R., et al. 2013, ApJ, 775, L36
 Kishimoto, M., Höning, S. F., Beckert, T., & Weigelt, G. 2007, A&A, 476, 713
 Kokubo, M. & Minezaki, T. 2020, MNRAS, 491, 4615
 Kollatschny, W. & Fricke, K. J. 1985, A&A, 146, L11
 Korista, K. T. & Goad, M. R. 2004, ApJ, 606, 749
 Koshida, S., Minezaki, T., Yoshii, Y., et al. 2014, ApJ, 788, 159
 Koss, M., Trakhtenbrot, B., Ricci, C., et al. 2017, ApJ, 850, 74
 Leftley, J. H., Tristram, K. R. W., Höning, S. F., et al. 2021, ApJ, 912, 96
 Lira, P., Arévalo, P., Uttley, P., McHardy, I., & Breidt, E. 2011, MNRAS, 415, 1290
 Lira, P., Arévalo, P., Uttley, P., McHardy, I. M. M., & Videla, L. 2015, MNRAS, 454, 368
 Lub, J. & de Ruiter, H. R. 1992, A&A, 256, 33
 Mandal, A. K., Rakshit, S., Kurian, K. S., et al. 2018, MNRAS, 475, 5330
 Mandal, A. K., Rakshit, S., Stalin, C. S., et al. 2021a, MNRAS, 501, 3905
 Mandal, A. K., Schramm, M., Rakshit, S., et al. 2021b, MNRAS, 508, 5296
 Marconi, A., Maiolino, R., & Petrov, R. G. 2003, Ap&SS, 286, 245
 Marin, F., Hutsemékers, D., & Agís González, B. 2019, in SF2A-2019: Proceedings of the Annual meeting of the French Society of Astronomy and Astrophysics, ed. P. Di Matteo, O. Creevey, A. Crida, G. Kordopatis, J. Malzac, J. B. Marquette, M. N'Diaye, & O. Venot, Di
 Martínez-Aldama, M. L., Czerny, B., Kawka, D., et al. 2019, ApJ, 883, 170
 Mejía-Restrepo, J. E., Lira, P., Netzer, H., Trakhtenbrot, B., & Capellupo, D. M. 2018, Nature Astronomy, 2, 63
 Minezaki, T., Yoshii, Y., Kobayashi, Y., et al. 2004, ApJ, 600, L35
 Minezaki, T., Yoshii, Y., Kobayashi, Y., et al. 2019, ApJ, 886, 150
 Nardini, E., Reeves, J. N., Gofford, J., et al. 2015, Science, 347, 860
 Netzer, H. 1990, in Active Galactic Nuclei, ed. R. D. Blandford, H. Netzer, L. Woltjer, T. J. L. Courvoisier, & M. Mayor, 57–160
 Oknyanskij, V. L., Lyuty, V. M., Taranova, O. G., & Shenavrin, V. I. 1999, Astronomy Letters, 25, 483
 Oknyansky, V. L., Gaskell, C. M., & Shimanovskaya, E. V. 2015, Odessa Astronomical Publications, 28, 175
 Onishi, K., Iguchi, S., Davis, T. A., et al. 2017, MNRAS, 468, 4663
 Onken, C. A., Ferrarese, L., Merritt, D., et al. 2004, ApJ, 615, 645
 Onken, C. A. & Peterson, B. M. 2002, ApJ, 572, 746
 Onken, C. A., Valluri, M., Brown, J. S., et al. 2014, ApJ, 791, 37
 Onori, F., Ricci, F., La Franca, F., et al. 2017, MNRAS, 468, L97

- Pan, X., Zhou, H., Yang, C., et al. 2021, *ApJ*, 912, 118
- Pancoast, A., Brewer, B. J., & Treu, T. 2014a, *MNRAS*, 445, 3055
- Pancoast, A., Brewer, B. J., Treu, T., et al. 2014b, *MNRAS*, 445, 3073
- Park, D., Kelly, B. C., Woo, J.-H., & Treu, T. 2012, *ApJS*, 203, 6
- Peterson, B. M. 1993, *PASP*, 105, 247
- Peterson, B. M. 2014, *Space Sci. Rev.*, 183, 253
- Peterson, B. M., Ferrarese, L., Gilbert, K. M., et al. 2004, *ApJ*, 613, 682
- Peterson, B. M., Wanders, I., Bertram, R., et al. 1998, *ApJ*, 501, 82
- Petrov, R. G., Malbet, F., Richichi, A., et al. 2001, *Comptes Rendus Physique*, 2, 67
- Planck Collaboration, Ade, P. A. R., Aghanim, N., et al. 2016, *A&A*, 594, A13
- Pozo Nuñez, F., Haas, M., Chini, R., et al. 2014, *A&A*, 561, L8
- Pozo Nuñez, F., Ramolla, M., Westhues, C., et al. 2015, *A&A*, 576, A73
- Prieto, A., Rodríguez-Ardila, A., Panda, S., & Marinello, M. 2022, *MNRAS*, 510, 1010
- Probst, M. A. & Kollatschny, W. 2020, *Contributions of the Astronomical Observatory Skalnaté Pleso*, 50, 360
- Ramolla, M., Haas, M., Westhues, C., et al. 2018, *A&A*, 620, A137
- Rashed, Y. E., Eckart, A., Valencia-S., M., et al. 2015, *MNRAS*, 454, 2918
- Rees, M. J., Silk, J. I., Werner, M. W., & Wickramasinghe, N. C. 1969, *Nature*, 223, 788
- Saglia, R. P., Opitsch, M., Erwin, P., et al. 2016, *ApJ*, 818, 47
- Senarath, M. R., Brown, M. J. I., Cluver, M. E., et al. 2021, *MNRAS*, 503, 2583
- Shangguan, J., Ho, L. C., & Xie, Y. 2018, *ApJ*, 854, 158
- Shankar, F., Bernardi, M., Richardson, K., et al. 2019, *MNRAS*, 485, 1278
- Shapovalova, A. I., Popović, L. Č., et al. 2019, *MNRAS*, 485, 4790
- Shen, Y. 2013, *Bulletin of the Astronomical Society of India*, 41, 61
- Shen, Y. & Ho, L. C. 2014, *Nature*, 513, 210
- Sitko, M. L., Sitko, A. K., Siemiginowska, A., & Szczerba, R. 1993, *ApJ*, 409, 139
- Sobrinho Figaredo, C., Haas, M., Ramolla, M., et al. 2020, *AJ*, 159, 259
- Stalin, C. S., Jeyakumar, S., Coziol, R., Pawase, R. S., & Thakur, S. S. 2011, *MNRAS*, 416, 225
- Suganuma, M., Yoshii, Y., Kobayashi, Y., et al. 2006, *ApJ*, 639, 46
- Swain, M., Vasisht, G., Akeson, R., et al. 2003, *ApJ*, 596, L163
- Thomas, J., Saglia, R. P., Bender, R., et al. 2004, *MNRAS*, 353, 391
- Vestergaard, M. & Peterson, B. M. 2006, *ApJ*, 641, 689
- Wang, J.-M., Du, P., Brotherton, M. S., et al. 2017, *Nature Astronomy*, 1, 775
- Williams, P. R., Pancoast, A., Treu, T., et al. 2018, *ApJ*, 866, 75
- Wittkowski, M., Kervella, P., Arsenault, R., et al. 2004, *A&A*, 418, L39
- Woo, J.-H., Treu, T., Barth, A. J., et al. 2010, *ApJ*, 716, 269
- Zheng, X. Z., Xia, X. Y., Mao, S., Wu, H., & Deng, Z. G. 2002, *AJ*, 124, 18
-
- ¹ Max Planck Institute for Extraterrestrial Physics (MPE), Giessenbachstr.1, 85748 Garching, Germany
- ² LESIA, Observatoire de Paris, Université PSL, CNRS, Sorbonne Université, Univ. Paris Diderot, Sorbonne Paris Cité, 5 place Jules Janssen, 92195 Meudon, France
- ³ I. Institute of Physics, University of Cologne, Zùlpicher Straße 77, 50937 Cologne, Germany
- ⁴ Departments of Physics and Astronomy, Le Conte Hall, University of California, Berkeley, CA 94720, USA
- ⁵ Department of Physics and Astronomy, University of Southampton, Southampton, UK
- ⁶ Department of Physics, Kyoto Sangyo University, Kita-ku, Japan
- ⁷ Université Côte d'Azur, Observatoire de la Côte d'Azur, CNRS, Laboratoire Lagrange, Nice, France
- ⁸ School of Physics and Astronomy, Tel Aviv University, Tel Aviv 69978, Israel
- ⁹ Univ. Grenoble Alpes, CNRS, IPAG, 38000 Grenoble, France
- ¹⁰ Center for Computational Astrophysics, Flatiron Institute, 162 5th Ave., New York, NY 10010, USA
- ¹¹ European Southern Observatory, Casilla 19001, Santiago 19, Chile
- ¹² European Southern Observatory, Karl-Schwarzschild-Str. 2, 85748 Garching, Germany
- ¹³ Sterrewacht Leiden, Leiden University, Postbus 9513, 2300 RA Leiden, The Netherlands
- ¹⁴ Max Planck Institute for Radio Astronomy, Auf dem Hügel 69, 53121 Bonn, Germany
- ¹⁵ Universidade de Lisboa - Faculdade de Ciências, Campo Grande, 1749-016 Lisboa, Portugal
- ¹⁶ Faculdade de Engenharia, Universidade do Porto, rua Dr. Roberto Frias, 4200-465 Porto, Portugal
- ¹⁷ CENTRA - Centro de Astrofísica e Gravitação, IST, Universidade de Lisboa, 1049-001 Lisboa, Portugal
- ¹⁸ Max Planck Institute for Astronomy, Königstuhl 17, 69117, Heidelberg, Germany
- ¹⁹ Instituto de Astrofísica de Canarias (IAC), E-38200 La Laguna, Tenerife, Spain
- ²⁰ Department of Astrophysical & Planetary Sciences, JILA, University of Colorado, Duane Physics Bldg., 2000 Colorado Ave, Boulder, CO 80309, USA
- ²¹ Research School of Astronomy and Astrophysics, Australian National University, Canberra, ACT 2611, Australia
- ²² Retired